

Mojtaba Mirdrikvand, Jan Ilsemann, Jorg Thöming, Wolfgang Dreher

Spatially resolved characterization of the gas propagator in monolithic structured catalysts using NMR diffusiometry

Journal Article as: peer-reviewed accepted version (Postprint)

DOI of this document\* (secondary publication): 10.26092/elib/2473

Publication date of this document: 11/09/2023

\* for better findability or for reliable citation

Recommended Citation (primary publication/Version of Record) incl. DOI:

Mojtaba Mirdrikvand, Jan Ilsemann, Jorg Thöming, Wolfgang Dreher  
Spatially resolved characterization of the gas propagator in monolithic structured catalysts using NMR diffusiometry ; Chemical engineering & technology, Volume 41, Issue 9, pages 1871-1880, <https://doi.org/10.1002/ceat.201800201>

Please note that the version of this document may differ from the final published version (Version of Record/primary publication) in terms of copy-editing, pagination, publication date and DOI. Please cite the version that you actually used. Before citing, you are also advised to check the publisher's website for any subsequent corrections or retractions (see also <https://retractionwatch.com/>).

"This is the peer reviewed version of the following article: [Mojtaba Mirdrikvand, Jan Ilsemann, Jorg Thöming, Wolfgang Dreher Spatially resolved characterization of the gas propagator in monolithic structured catalysts using NMR diffusiometry ; Chemical engineering & technology, Volume 41, Issue 9, pages 1871-1880, <https://doi.org/10.1002/ceat.201800201>], which has been published in final form at [<https://doi.org/10.1002/ceat.201800201>]. This article may be used for non-commercial purposes in accordance with Wiley Terms and Conditions for Use of Self-Archived Versions. This article may not be enhanced, enriched or otherwise transformed into a derivative work, without express permission from Wiley or by statutory rights under applicable legislation. Copyright notices must not be removed, obscured or modified. The article must be linked to Wiley's version of record on Wiley Online Library and any embedding, framing or otherwise making available the article or pages thereof by third parties from platforms, services and websites other than Wiley Online Library must be prohibited."

This document is made available with all rights reserved.

Take down policy

If you believe that this document or any material on this site infringes copyright, please contact [publizieren@suub.uni-bremen.de](mailto:publizieren@suub.uni-bremen.de) with full details and we will remove access to the material.

# Spatially Resolved Characterization of the Gas Propagator in Monolithic Structured Catalysts Using NMR Diffusiometry

Gas diffusivity measurements in opaque porous media were performed using nuclear magnetic resonance. An optimized pulsed-field gradient stimulated echo method with free volume selection was used to investigate the propagator of thermally polarized methane gas within commercial monolithic catalyst supports. Since signal losses due to  $T_2$  relaxation were minimized by using a short echo time, diffusion processes could be characterized by the measured propagator functions and effective diffusion coefficients were determined for a broad range of observation times and in different spatial directions. The study of this noninvasive characterization of gas diffusion found a clear effect of the monolith type and its pore size and coating on the effective gas diffusion coefficient and the apparent tortuosity for a given observation time.

**Keywords:** Diffusion, Heterogeneous catalysis, Propagator, Thermally polarized gas, Tortuosity

*Received:* April 24, 2018; *revised:* June 20, 2018; *accepted:* July 16, 2018

**DOI:** 10.1002/ceat.201800201

## 1 Introduction

Nuclear magnetic resonance (NMR) provides a fascinating research field for measuring static and dynamic properties of porous structures. In particular, when the thermophysical behavior of gases and the translational motion of the molecules in porous structures such as catalyst carriers are considered, the implementation of a robust in situ measuring technique is of high importance [1–4]. In porous media, pore surfaces play a significant role in the restriction or hindrance of diffusion. This causes a change in the diffusion coefficient  $D$  of the guest molecules inside the structure, resulting in the effective diffusion coefficient  $D_{\text{eff}}$ .<sup>1)</sup> Although optical in situ techniques reveal information on some transport properties in porous media at the molecular level, they are limited to optically accessible systems and unable to measure self-diffusion [2]. NMR, however, is suitable to measure also in case of opaque systems such as catalyst pellets and open porous foams. Moreover, the flexibility of NMR, which allows the combination of spatial resolution with diffusiometry, relaxometry, or spectroscopy, makes spatially resolved NMR measurements even more attractive, allowing a better understanding of the effect of geometry on mass transport in porous structures. It is worth mentioning that NMR diffusiometry enables the detection of the spatial displacement of molecules far below the spatial resolution obtained in magnetic resonance imaging (MRI) or spatially resolved NMR spectroscopy [5, 6].

The application of monolithic ceramic catalyst supports has tremendously grown in recent years [7]. The interconnected network of ceramic sponges named as foams offers enhanced heat transfer properties and less pressure drop as compared to packed beds [7–9]. Therefore, it is promising to use NMR techniques to investigate the effect of the pore window size and struts on the propagator function of gases in catalytic gas phase systems.

Recently, some NMR-based morphological studies of regular and irregular monolithic structures have been reported [10–21]. Grosse et al. [12] investigated the porosity, pore size distribution, and other properties of heterogeneous structures. They described a volume-selective NMR imaging study on ceramic sponges to determine the pore size distribution. In another study, van Gulijk et al. [10] pointed out that NMR analysis of gaseous flow in honeycomb channels would be expensive and time consuming compared to local pressure

---

<sup>1</sup>Mojtaba Mirdrikvand, Dr. Wolfgang Dreher  
mirdrikvand@uni-bremen.de

University of Bremen, Department of Chemistry, In vivo MR Group, Leobener Strasse 7, 28359 Bremen, Germany.

<sup>2</sup>Jan Ilsemann  
University of Bremen, Institute of Applied and Physical Chemistry, Department of Chemistry, Leobener Strasse 6, 28359 Bremen, Germany.

<sup>3</sup>Prof. Jorg Thöming  
University of Bremen, Center of Environmental Research and Sustainable Technology (UFT), Leobener Strasse 6, 28359 Bremen, Germany.

---

1) List of symbols at the end of the paper.

drop measurements. In case of irregular pore structures, however, such local pressure drop measurements are impossible. Codd and Altobelli [1] showed, in their case study on glass spheres with a diameter of 300–500  $\mu\text{m}$ , that diffusion and flow measurements by NMR can facilitate the investigation of porous structures. Their work confirmed that a global gas propagator analysis yields structural information for a chosen observation time [1, 2, 11]. Lysova et al. [13] and Koptyug et al. [14] performed NMR measurements for studying structured catalysts and related transport phenomena in liquids and gases. Changes in the structures of the catalyst supports over the operating time of the reactor can also be evaluated [14]. A similar approach, but in the liquid phase and not spatially resolved, was used by Ren et al. [15] on deactivated catalyst samples to show the self-diffusion and tortuosity in naphtha-reforming catalyst pellets by  $^1\text{H}$  NMR on heptane. In addition, Youngs et al. [16] applied pulsed-field gradient (PFG)-NMR for studying the diffusion of liquid isopropanol in an alumina structure to show the interaction of molecules with the surface of the alumina.

NMR of thermally polarized gases is more challenging in comparison with that of liquids, due to reduced spin density, faster movements of the molecules, and the short transversal relaxation time  $T_2$ , which cause a considerably reduced signal-to-noise ratio (SNR) in gas phase NMR [1, 17, 18]. As a solution, studies on hyperpolarized gases have been published [22]. Although hyperpolarization is a powerful approach, the study of thermally polarized gases is also attractive because the rather expensive hyperpolarization techniques as well as the inherent signal losses by  $T_1$  relaxation during longer experiments are avoided. Additionally, the rather short  $^1\text{H}$  NMR spin-lattice relaxation time  $T_1$  of thermally polarized gases allows the use of short repetition times (TR) leading to an improved SNR per unit measurement time. Beyea et al. [23] showed the advantage of measuring thermally polarized gases in porous structures in some instances on yttria-stabilized zirconia (Y-TZP) ceramic samples and lungs. Additionally, flow studies on hydrogen-containing gases in supported catalysts have been performed by Koptyug et al. [24], but to the best of our knowledge, a spatially resolved study on the diffusion of thermally polarized gases in monolithic structures with different pore sizes has not yet been reported.

In our work, we demonstrate that such a quantitative analysis can be performed by optimized NMR diffusometry within a moderate measurement time. The mass transport properties of different monolithic catalyst supports were determined using optimized NMR sequences with a customizable volume of interest, offering a spatially

resolved detection of the gas propagator in monolithic structures. These measurements can answer the question as to which extent self-diffusion of gas molecules varies for different diffusion times and along different spatial directions. Besides, the study was performed on coated and uncoated structures of irregular and regular monolithic supports to reveal characteristic differences that are relevant for practical applications. The results can also be used for validating the numerical simulation of heterogeneous gas phase systems both on the micro and the macro level.

## 2 Theory and Method

### 2.1 PFG-STE Measurements

Since Stejskal and Tanner have proposed PFG-NMR experiments for determining diffusion coefficients, spin echo (SE)-[4] or stimulated echo (STE)-based [25] PFG-NMR measurements have been used in numerous applications [26, 27]. STE pulse sequences exhibit an inherent 50% SNR loss as compared to SE pulse sequences, because signal refocusing is performed by  $90^\circ$  radio frequency (RF) pulses, and not by  $180^\circ$  RF pulses as in SE sequences (see Fig. 1). However, STE-based approaches are often preferred for diffusion studies to minimize relaxation losses (see Eq. 2). In particular, this applies to gas phase  $^1\text{H}$  NMR because short spin-spin relaxation times  $T_2$  are found in most cases, while the spin-lattice relaxation time  $T_1$  is much longer than  $T_2$  [27, 28].

A volume-selective STE pulse sequence [29, 30] was implemented on our 7-Tesla (7T) MRI system to restrict the measurements to a volume element (voxel) with well-defined size and arbitrary voxel orientation. As proposed by Tkáč et al.

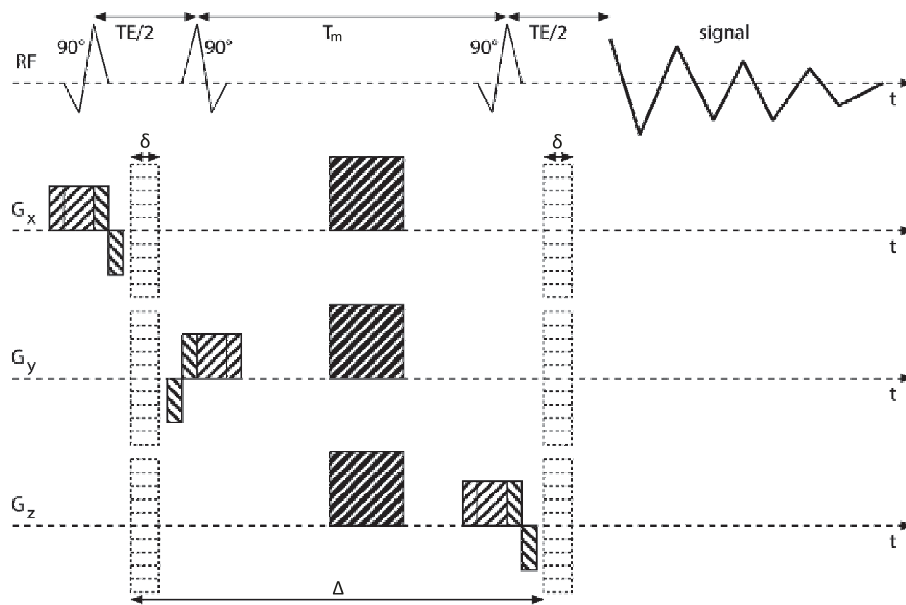


**Figure 1.** Scheme of the optimized PFG-STE imaging sequence (not to scale) used for localized  $q$ -space measurements. During the mixing time  $T_m$ , spoiler gradients are applied to suppress unwanted coherence pathways. A two-step phase cycle ( $0^\circ$ – $180^\circ$ ) was applied for the third  $90^\circ$  pulse to suppress the signal excited by this RF pulse.

[31], asymmetric RF pulses were used for reducing the minimum echo time (TE) and thus signal losses by  $T_2$  relaxation. Diffusion-sensitizing gradients of arbitrary orientation can be applied between the first and the second RF pulse as well as between the third RF pulse and the start of data acquisition. A scheme of the pulse sequence is shown in Fig. 1, with  $\delta$  being the duration and  $G_d$  the resulting amplitude of the two diffusion-sensitizing gradient pulses applied in  $x$ -,  $y$ -, and  $z$ -direction, and  $\Delta$  being the delay between these gradient pulses. Note that during the mixing time  $T_m$ , i.e. between the second and the third RF pulse, the magnetization experiences only  $T_1$  relaxation, thus allowing measurements with a rather long diffusion time.

Assuming Gaussian diffusion, the diffusion coefficient  $D$  can be determined by two or more measurements performed with different diffusion weighting expressed by the so-called  $b$ -value, but with constant TE and  $T_m$ :

$$b = \gamma^2 \delta^2 G_d^2 \left( \Delta - \frac{\delta}{3} \right) \quad (1)$$

The amplitude of the measured STE signal is given by

$$S = S_0 e^{-\frac{TE}{T_2}} e^{-\frac{T_m}{T_1}} e^{-bD} \quad (2)$$

In the more general approach of ‘ $q$ -space imaging’ proposed by Cory and Garroway [32] as well as Callaghan et al. [33], a series of measurements is performed by incrementing the  $q$ -values defined by  $q = \gamma \delta G_d$ . If  $\delta \ll \Delta$ , the echo signal is given by

$$S(q) = \int \rho(r_0) \int P(r_0|r, \Delta) e^{iq(r-r_0)} dr dr_0 \quad (3)$$

Here  $r_0$  and  $r$  denote the positions of the spins at the beginning and the end of the observation, respectively, i.e., the diffusion time  $\Delta$ . Thus, the displacement function  $P$ , averaged over the measured sample, can be determined by Fourier transformation of the measured data  $S(q)$ .  $P$  describes the probability that spins have moved during the observation time  $\Delta$  by the distance  $r - r_0$  along the direction of the diffusion gradients.

In case of Gaussian diffusion, the diffusion coefficient  $D$  can be determined from the full-width half maximum (FWHM) value of the gas propagator using

$$D = (FWHM)^2 / (16 \ln(2) \Delta) \quad (4)$$

However, note that rather small differences in FWHM values result in large differences in the diffusion coefficient.

The transition from free to increasingly hindered diffusion can be observed by performing measurements with increasing  $\Delta$ . Considering spherical pores with radius  $a$  as a simple model, the dimensionless parameter  $\varepsilon = D\Delta/a^2$  helps to distinguish three time regimes [2]: (i) a short observation time for  $\varepsilon \ll 1$  corresponding to free diffusion and yielding the free diffusion coefficient  $D_0$ , (ii) a ‘crossover’ regime for  $\varepsilon \approx 1$ , in which a certain number of the particles will experience restrictions such as reflections on the pore surface, and (iii) a long observation time if  $\varepsilon \gg 1$ , where for hindered diffusion the diffusion coefficient

determined for increasing  $\Delta$  converges to the value  $D_\infty$ . The tortuosity, interpreted as a path length multiplication factor in the long observation time regime, can be calculated by  $D_0/D_\infty$ . The transition from the crossover regime to the long observation time regime and the corresponding increase in the path length multiplication factor can be characterized by measuring  $D_0/D_{\text{eff}}$  as a function of the diffusion time, corresponding to an apparent tortuosity for a given observation time.

## 3 Experimental

### 3.1 Materials

Four different  $\text{Al}_2\text{O}_3$ -sponge segments (length: 23 mm, diameter: 25 mm, 10, 20, 30, or 40 pores per inch (PPI); Drache GmbH, Diez, Germany) were used as raw ceramic sponges, and a cordierite honeycomb monolith (length: 38 mm, diameter: 25 mm, 600 cells per square inch (cpsi); NGK, Poland) was used as monolithic catalyst support. The morphological characteristics of the samples are given in Tab. 1.

**Table 1.** Properties of the used sponges [39].

| PPI | Window diameter [mm] | Strut diameter [mm] | Open porosity $\xi$ | Surface area [ $\text{m}^2\text{m}^{-3}$ ] |
|-----|----------------------|---------------------|---------------------|--|
| 10  | $3.30 \pm 0.98$      | 1.83                | 0.77                | 521.3                                      |
| 20  | $2.04 \pm 0.48$      | 1.22                | 0.75                | 852.3                                      |
| 30  | $1.92 \pm 0.46$      | 1.11                | 0.76                | 862.5                                      |
| 40  | $1.43 \pm 0.39$      | 0.73                | 0.79                | 1105.8                                     |

The sponge with 20 PPI and the honeycomb were coated as described below (Sect. 3.2). Methane was used as probing gas because this molecule is of particular interest in our current research on methanation reactions. The samples were positioned in a batch glass tube container (length: 250 mm, diameter: 25 mm) equipped with a pressure valve for the filling process.

Special valves and O-rings (Schott AG, Germany) were used, and leakage tests were conducted to ensure that the gas container was completely sealed.

The gas filling was conducted using a flow meter (One OMEGA FMA-2605; OMEGA Engineering, Norwalk, USA). The pressure in the gas mouse was set to 1.5 bar and the temperature during the NMR measurements was 16 °C. The temperature was monitored during all NMR measurements. The gas container was held firmly within the RF coil in order to prevent motional artifacts.

### 3.2 Catalyst Preparation

All monolithic substrates were coated with a 6-wt % Ni/ $\text{Al}_2\text{O}_3$  catalyst layer. Nickel nitrate hexahydrate (Prolabo; 97 %) was dissolved in deionized water and mixed with an aqueous

$\gamma$ -Al<sub>2</sub>O<sub>3</sub> slurry. The substrates were dipped into the mixed slurry, and excessive material was subsequently blown off using compressed air. Then the coated samples were dried at 393 K for 1 h and further calcined at 873 K for 2 h (heating ramp 1 K min<sup>-1</sup>). Comparing the weights of the uncoated and calcined samples, the amount of coating material was determined to be approximately 3.6 g for the honeycomb sample and 1.7 g for the sponge. By evaporation of the liquid phase, the solid fraction of the slurry was determined to be 43.4%. In order to achieve a loading of 6 wt % Ni, 17.94 g of Ni(NO<sub>3</sub>)<sub>2</sub>·6H<sub>2</sub>O was dissolved in 16 mL deionized H<sub>2</sub>O.

N<sub>2</sub> physisorption measurements were conducted using a NOVA 4000e gas sorption system (Quantachrome Instruments, Boynton Beach, FL, USA) to determine the pore size distribution. Prior to each analysis, the powders were degassed at 473 K for at least 2 h, whereas the subsequent isotherm measurements were conducted at 77 K for a relative pressure  $p/p_0$  in the range of 0.1–0.99.

### 3.3 NMR Measurements

#### 3.3.1 Hardware

All NMR experiments were performed on a 7T preclinical NMR imaging system (Biospec 70/20; Bruker Biospin GmbH, Ettlingen, Germany) equipped with the gradient system BGA12S2 (maximum gradient strength: 441 mT m<sup>-1</sup> in each direction, rise time: 130  $\mu$ s). A quadrature birdcage RF coil (inner diameter: 72 mm) was used for RF excitation and signal detection. The NMR pulse sequences were implemented using Paravision 5.1.

#### 3.3.2 MRI

To define the orientation of the samples and to position the voxel for subsequent PFG-NMR measurements, an optimized 3D gradient echo [29] imaging sequence was used with the following protocol: TR: 25 ms, TE: 0.5 ms, flip angle: 45°, field-of-view (FOV): 64 × 64 × 96 mm<sup>3</sup>, 192 × 192 × 16 matrix size, two averages, total measurement time: 2 min 33 s.

#### 3.3.3 Localized PFG-NMR

Localized measurements of displacement profiles were performed with an optimized PFG-STE sequence (Fig. 1). Rephasing or dephasing gradients were applied immediately after or prior to the slice-selective RF pulses, respectively, to minimize the diffusion weighting. To suppress unwanted signals, spoiler gradients were employed during the mixing time  $T_m$ , and a two-step phase cycle (0°–180°) for the third 90° pulse was used. The pulse sequence was used with the following parameters: asymmetric 90° RF pulses of 500  $\mu$ s duration calculated by the RF pulse module of the free software suite VESPA [34] (version 0.8, <http://scion.duhs.duke.edu/vespa/project>), voxel size: 12 × 12 × 12 mm<sup>3</sup>, TR = 250 ms, 64 equidistant  $q$ -space values, displacement range  $\pm 5$  mm, 1024 complex data points sampled

with 25 kHz. Measurements were performed with a TE of 2.6 ms and diffusion times  $\Delta$  ranging from 3.51 to 50 ms. For each set of parameters, six measurements were performed for error estimation and improved accuracy. Optionally, the data sets were averaged to increase the SNR. Three measurements were conducted for each observation time using diffusion sensitizing gradients in  $x$ -,  $y$ -, or  $z$ -direction, where  $z$  corresponds to the axial direction of cylindrical samples. The measurement time for each measurement was 8 min 23 s.

#### 3.3.4 Data Evaluation

The time domain signals were analyzed using self-written MATLAB (R2017b; The MathWorks, Inc., Natick, MA, USA) scripts. The propagator was calculated from the time domain signal applying the following steps: Hamming apodization, one-dimensional (1D) Fourier transformation along the time domain, magnitude calculation, peak integration, and subsequent 1D Fourier transformation along the variable  $q$ . Note that magnitude calculation avoids phase errors during phase correction of Fourier transform spectra, but suppresses flow effects overlaid on diffusion processes. However, flow is not expected for the current experimental setup.

## 4 Results and Discussion

The results are presented in two main parts. First, we analyzed the raw regular and irregular monolithic structures. While the spatial dependence of the gas propagator was studied for the regular structure, the gas propagator was compared between irregular samples with 10, 20, 30 and 40 PPI, and the effective diffusion constants and the apparent tortuosity values were determined at diffusion times from 3.5 to 30 ms. Second, the differences in gas diffusion between coated and uncoated honeycomb and sponge samples were analyzed.

Before measuring diffusion in porous structures, the diffusion coefficients of free methane (16 °C, 1.5 bar) was determined. The value of  $(2.24 \pm 0.006) \times 10^{-5}$  m<sup>2</sup>s<sup>-1</sup> is in good agreement with the literature value [35] and remained unchanged after several weeks, proving the tightness of the gas container. In addition, the Brunauer-Emmett-Teller (BET) surface area of the coated catalyst is found to be 135 m<sup>2</sup>g<sup>-1</sup> with a total pore volume of 0.44 cm<sup>3</sup>g<sup>-1</sup>. The pore size distribution was calculated by the Barrett-Joyner-Halenda (BJH) model using the desorption branch, showing a maximum at a radius of 4.1 nm (see the Supporting Information).

### 4.1 Raw Honeycomb Structure

The propagators of methane gas in the raw honeycomb are illustrated in Fig. 2. The measurements were conducted with short (5 ms; Fig. 2 a) and long (30 ms; Fig. 2 b) diffusion times. A Gaussian fit is superimposed as a reference, indicating possible effects of hindered or restricted diffusion. Along the longitudinal direction, the diffusion coefficient and the displacement function of the gas were close to the results obtained for freely

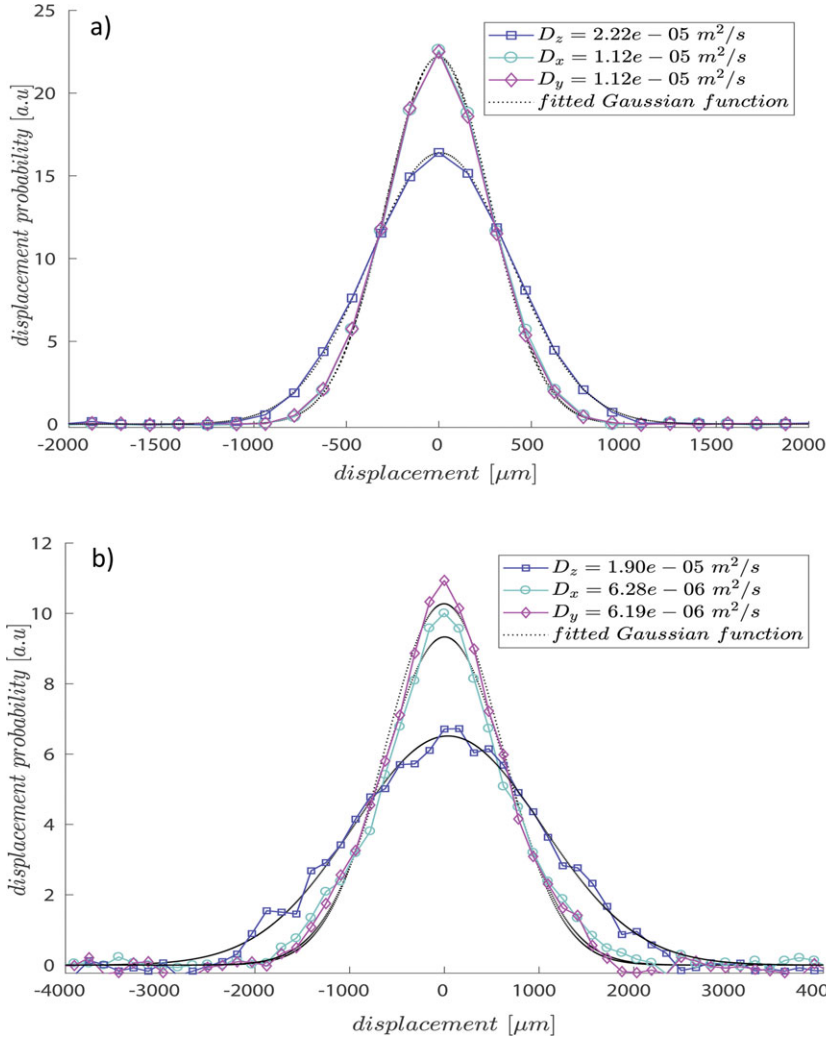


**Figure 2.** The propagators represent the methane gas displacement function in the 600-cpsi honeycomb monolith at (a)  $\Delta = 5$  ms and (b)  $\Delta = 30$  ms. For comparison, a fitted Gaussian function is overlaid in the same color as used for the measured data.

diffusing gas, slightly affected by the channel-like structure of the honeycomb.

At short diffusion time ( $\Delta = 3.5$  ms), the diffusion coefficient of gas in the longitudinal direction is  $D = (2.22 \pm 0.03) \times 10^{-5} \text{ m}^2\text{s}^{-1}$ , showing a difference of  $< 1\%$  from the free-gas value. The diffusion coefficient remains almost constant in the longitudinal direction, even in long diffusion time measurements ( $\Delta = 30$  ms) where  $D = (2.11 \pm 0.01) \times 10^{-5} \text{ m}^2\text{s}^{-1}$  was calculated. The fact that the effective diffusion coefficient is almost independent of the diffusion time is due to unrestricted motion of gas molecules along the  $z$ -axis, and the minor reduction in the diffusion coefficient can be explained by reflected or stagnant gas molecules at the channel walls in the honeycomb. Conversely, in the transversal direction, a significantly narrower curve shows more restricted gas displacement behavior. According to the intrinsic square-like channels of the honeycomb sample, both transversal (in  $x$  and  $y$ ) measurements yield similar but lower diffusion coefficients. At longer diffusion time, where more

interactions between gas molecules and the walls of the honeycomb channels are expected, the methane propagator shows a remarkable deviation from the fitted Gaussian curve (Fig. 2 b). The averaged values for the gas diffusion coefficient in the transversal direction were  $D = (1.12 \pm 0.008) \times 10^{-5} \text{ m}^2\text{s}^{-1}$  and  $(6.26 \pm 0.2) \times 10^{-6} \text{ m}^2\text{s}^{-1}$ , for the short and the long diffusion time, respectively. It is remarkable that the largest displacements of the gas molecules observed in transversal direction at  $\Delta = 30$  ms are larger than the width of the honeycomb channel length (1 mm), meaning that the gas molecules are still visible in the measurements after having crossed the channel walls.

## 4.2 Analysis of Sponge Samples with Different Pore Densities

Sponges with different pore densities were analyzed in order to show the differences in the diffusion coefficient of the probing gas and to determine the apparent tortuosity of the catalyst supports. While Tab. 2 gives the diffusion coefficients in  $x$ -,  $y$ -, and  $z$ -direction, an average value is depicted on each graph in Fig. 3. Although the average values for the diffusion coefficients for the propagators in Fig. 3 suppress the anisotropic behavior of the diffusion process in the porous sample, they represent the average properties of the samples based on their pore density and heterogeneity.

At short diffusion times (3.5 ms), the propagators of all sponges show hindered motion influenced by the pore walls, resulting in narrower peaks compared to the propagator measured for the free gas. Even at this rather short diffusion time, the sponges with higher pore density are already considerably affected by the interaction with the pore walls. Only the 10-PPI sponge shows less hindrance and thus smaller differences to the data from the free gas. This remaining difference can also be recognized by comparing the baselines of the displacement functions of the free gas and the 10-PPI sample. The displacement function of the free gas reaches the baseline at  $\sim 1.5$  mm at 3.5 ms diffusion time (Fig. 3 a), while the gas propagator of the 10-PPI sample reaches the baseline at  $\sim 1.2$  mm. These findings are consistent with the different values of the window diameters of the samples (see Tab. 1), which is 3.3 mm for the 10-PPI sample, explaining the observed differences from the propagator of the free gas. The smaller window size of pores in the 20-, 30- and 40-PPI samples hinders the gas more than in the 10-PPI sponge, resulting in narrower propagators and smaller diffusion coefficients (see Tab. 2). Although, at a first glance, the gas propagators of samples possessing higher pore density values (20, 30, and 40 PPI) seem to

**Table 2.** Effective diffusion coefficients ( $D_{\text{eff},i} \times 10^5$ , in  $\text{m}^2\text{s}^{-1}$ ) versus diffusion times.<sup>a)</sup>

| $\Delta$ | 10 PPI             |                    |                    | 20 PPI             |                    |                    | 30 PPI             |                    |                    | 40 PPI             |                    |                    |
|----------|--------------------|--------------------|--------------------|--------------------|--------------------|--------------------|--------------------|--------------------|--------------------|--------------------|--------------------|--------------------|
|          | $D_{\text{eff},z}$ | $D_{\text{eff},x}$ | $D_{\text{eff},y}$ |
| 3.5 ms   | $1.96 \pm 0.01$    | $2.01 \pm 0.02$    | $2.01 \pm 0.02$    | $1.79 \pm 0.02$    | $1.87 \pm 0.01$    | $1.87 \pm 0.01$    | $1.74 \pm 0.01$    | $1.84 \pm 0.01$    | $1.83 \pm 0.01$    | $1.69 \pm 0.01$    | $1.79 \pm 0.01$    | $1.74 \pm 0.02$    |
| 5 ms     | $1.91 \pm 0.02$    | $1.96 \pm 0.02$    | $1.96 \pm 0.02$    | $1.68 \pm 0.02$    | $1.78 \pm 0.03$    | $1.78 \pm 0.03$    | $1.63 \pm 0.02$    | $1.77 \pm 0.01$    | $1.73 \pm 0.01$    | $1.59 \pm 0.01$    | $1.71 \pm 0.01$    | $1.66 \pm 0.01$    |
| 10 ms    | $1.73 \pm 0.02$    | $1.82 \pm 0.02$    | $1.82 \pm 0.01$    | $1.53 \pm 0.05$    | $1.63 \pm 0.04$    | $1.63 \pm 0.02$    | $1.45 \pm 0.02$    | $1.61 \pm 0.02$    | $1.59 \pm 0.02$    | $1.48 \pm 0.03$    | $1.61 \pm 0.04$    | $1.51 \pm 0.02$    |
| 20 ms    | $1.52 \pm 0.02$    | $1.65 \pm 0.06$    | $1.63 \pm 0.02$    | $1.34 \pm 0.07$    | $1.47 \pm 0.07$    | $1.56 \pm 0.05$    | $1.32 \pm 0.09$    | $1.51 \pm 0.07$    | $1.43 \pm 0.04$    | $1.42 \pm 0.02$    | $1.61 \pm 0.07$    | $1.42 \pm 0.06$    |
| 30 ms    | $1.46 \pm 0.06$    | $1.52 \pm 0.07$    | $1.62 \pm 0.11$    | $1.32 \pm 0.15$    | $1.38 \pm 0.15$    | $1.40 \pm 0.10$    | $1.34 \pm 0.05$    | $1.46 \pm 0.10$    | $1.36 \pm 0.04$    | $1.45 \pm 0.09$    | $1.61 \pm 0.08$    | $1.36 \pm 0.10$    |

<sup>a)</sup> The values state the computed diffusion coefficients along the spatial directions  $i = z, x$ , and  $y$  for sponge samples with 10–40 PPI.

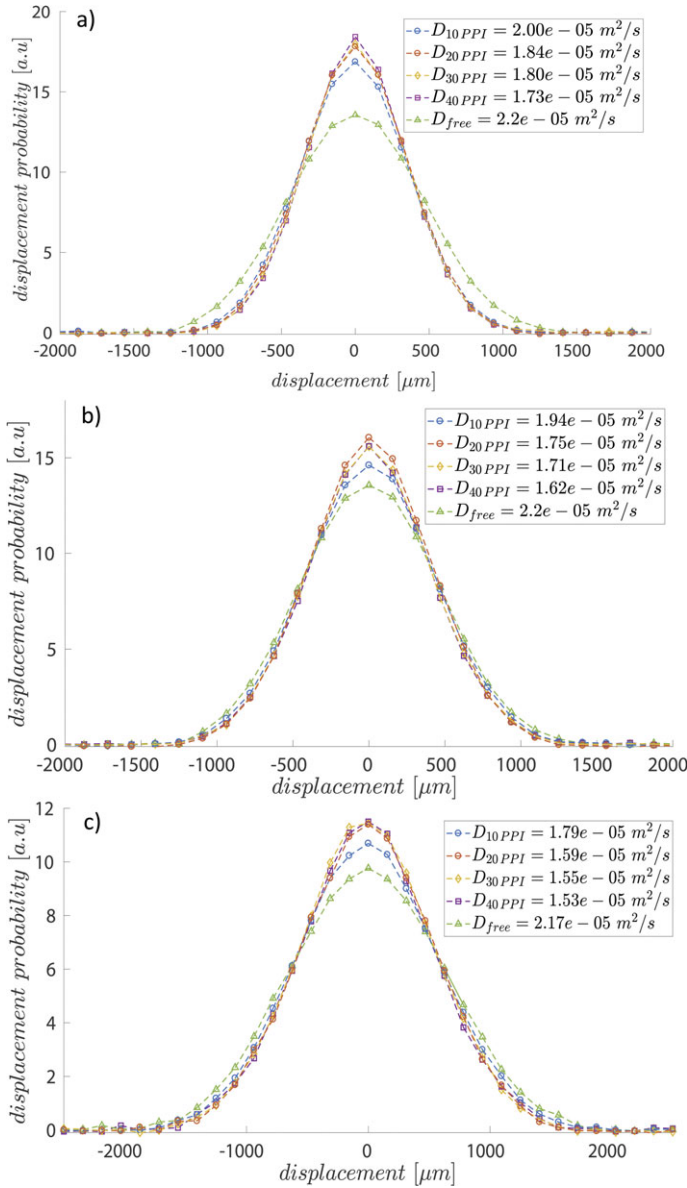


**Figure 3.** Gas displacement function for irregular monolithic structures at (a)  $\Delta = 3.5$  ms, (b)  $\Delta = 5$  ms and (c)  $\Delta = 10$  ms. Average values of diffusion coefficients are added to the figures for comparison.

be almost identical, some differences appear in the determined FWHM values of their displacement functions. In addition, at diffusion times of 5–10 ms, the gas molecules in the 10-PPI sample show broader displacement compared with the other sponges (20–40 PPI) (Fig. 3 b, c).

As shown in Tab. 2, the diffusion coefficient is decreased for the samples of higher pore density at each observation time. Thus, the highest and lowest diffusion coefficients belong to the 10-PPI and the 40-PPI samples, respectively. As an example for the trend of diffusion coefficient versus diffusion time, Fig. 4 shows the diffusion coefficients measured in  $y$ -direction. For all sponges, the observed effective diffusion coefficient decreases steadily with increasing diffusion time, converging to different  $D_\infty$  values. Already at a short observation time (3.5 ms), the gas propagators are affected by the macroscopic morphology of the sponges. As expected, the diffusion process is more influenced in the samples with smaller pore sizes, not only in the  $y$ -direction (Fig. 4), but in all directions (Tab. 2;  $\Delta = 20$ –30 ms). For longer diffusion times, the effect of different mean pore densities of the sponges increases with increasing diffusion time. Consequently, the diffusion coefficients decrease with longer observation times (Fig. 4). At diffusion times of  $\Delta = 20$ –30 ms, the time dependence of the diffusion coefficients starts to reach a plateau. This behavior can be regarded as a consequence of both the long interconnected pore network and the related tortuosity [1].

It should be emphasized that each individual sample has its inherent geometrical properties and tortuosity. These inherent properties in the geometry result from the fabrication process and the sintering of the ceramics green body, which may cause some deviations in the diffusion coefficient for different samples and along different directions. In addition, the measurement error increases with increasing diffusion time due to reduced SNR.

The determined diffusion coefficients of the 20- and 30-PPI samples have similar values at each observation time. This can be due to the rather similar strut diameters of these structures, where the strut diameter of the 20-PPI sample (1.11 mm) is in close proximity to the strut diameter of the 30-PPI (1.22 mm) sponges (see Tab. 1).

The spatially resolved diffusion measurements reveal information about the structure of the ceramic sponges. The method has the flexibility of characterizing an arbitrary

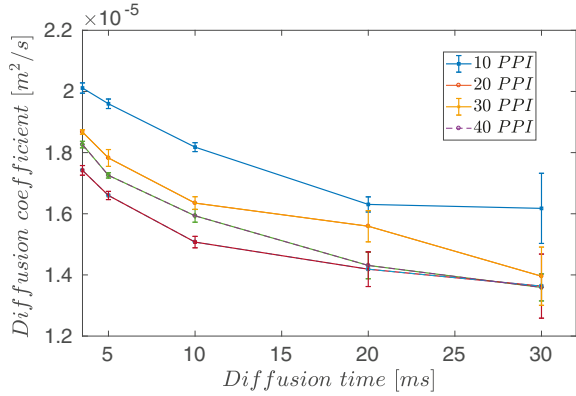


**Figure 4.** Plot of the effective diffusion coefficient in  $y$ -direction in ceramic sponges versus the diffusion time.

bitrary voxel element of the sample. Thus, in the future, more systematic diffusion studies on a sample can be done (i.e., center versus the edges of the sample). Another advantage of the method is that it is a non-destructive approach using a thermally polarized gas as probing material. Therefore, the characterized structure remains unchanged, which facilitates the analysis of the sample by measurements after certain operating times. Based on this, the alteration of the sample can be quantified before and after the operation. Another interesting application of the current method are measurements on hierarchically supported catalysts, where the spatially resolved approach of the technique may extract important information from these structures. Furthermore, using a gas as probing material with its inherently large diffusion lengths, as done in the presented measurements, allows diffusion studies and the determination of the apparent tortuosity of samples with rather large pores (millimeter range). Such measurements are not possible with liquids because of the limited diffusion lengths (micrometer range).

### 4.3 Tortuosity

The tortuosity  $\tau$  describes the order of hindrance in the sponges as a path length factor [1, 36]. Previously, some values were reported for the tortuosity of 45-PPI sponges in the range between 1.4 and 1.6 using computational fluid dynamics (CFD) [37]. Another study on solid metal sponges using a numerical approach has estimated the tortuosity for the sponges in the range from 1.179 to 1.208. In their study, no clear effect of the pore size on the tortuosity was found [38]. Although usually a constant value is reported for the long diffusion time limit, an apparent tortuosity can also be defined dependent on the observation time. This approach facilitates observing the transition from free diffusion to hindered diffusion caused by interaction of the gas molecules with the pore walls. This transition is of great interest for characterizing solid-gas systems,

in which both diffusion and flow determine the displacement function.

As the diffusion process in the sponges is influenced by the local heterogeneity and pore distribution, we measured the apparent tortuosity at each diffusion time. The measured values show the effect of the macroscopic structure on the transport phenomena in the sponges (Tab. 3). An average diffusion coefficient  $D_{\text{eff}}$  was calculated for each sponge according to the reported values for three spatial directions in Tab. 2. The diffusion coefficient of free gas was also measured at each observation time  $\Delta$ , and the apparent tortuosity was calculated by  $D_0/D_{\text{eff}}$ . However, the spatially resolved approach of the current method allows the investigation of local apparent tortuosity to extract more information about the topology of the volume of interest. Furthermore, the apparent tortuosity can be measured along different directions of the sponges based on the obtained diffusion coefficients (see Tab. 2) in order to show the effect of the macroscopic structure of the samples on the apparent tortuosity in an arbitrary direction.

**Table 3.** Apparent tortuosity for the sponge structures determined at various observation times.

|                         | $\Delta = 5$ ms | $\Delta = 10$ ms | $\Delta = 20$ ms | $\Delta = 30$ ms |
|-------------------------|-----------------|------------------|------------------|------------------|
| $\tau_{10 \text{ PPI}}$ | 1.16            | 1.21             | 1.40             | 1.50             |
| $\tau_{20 \text{ PPI}}$ | 1.27            | 1.32             | 1.50             | 1.65             |
| $\tau_{30 \text{ PPI}}$ | 1.30            | 1.36             | 1.55             | 1.64             |
| $\tau_{40 \text{ PPI}}$ | 1.35            | 1.39             | 1.52             | 1.56             |

### 4.4 Analysis of Coated Structures

An investigation of coated and uncoated honeycomb and sponge samples was conducted to show the differences between the propagators of both structures. The gas propagators of the raw and coated honeycomb structures are depicted Fig. 5 for comparison. The diffusion time was  $\Delta = 10$  ms for both samples. Measurements show a remarkable difference between the obtained gas diffusion coefficients along the transversal directions. The diffusion coefficients show a reduction by 37–40 %

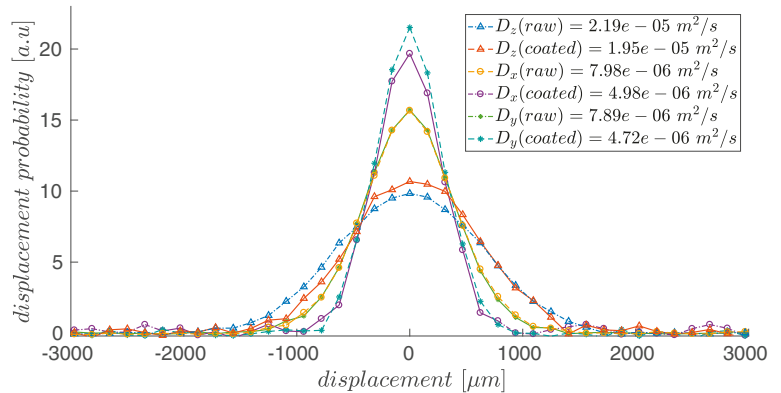


**Figure 5.** Displacement function of methane gas in coated and uncoated honeycomb monoliths at  $\Delta = 10$  ms.

in the coated sample along the transversal direction compared to the raw honeycomb. In addition, the comparison between the baseline values of the propagators in radial direction shows  $\sim 500\mu\text{m}$  gas displacement difference between the coated and uncoated samples. The narrower peak at zero shows a bigger fraction of trapped methane molecules in the coated honeycomb along each direction (Fig. 5). In  $z$ -direction, the difference between the gas propagators for the coated and uncoated honeycomb is smaller, but the diffusion coefficient is reduced by  $\sim 10\%$  in the coated sample.

The same approach was applied to the coated and uncoated 20-PPI sponge samples using  $\Delta = 5\text{ ms}$  and  $\Delta = 10\text{ ms}$ . A significant difference between the displacement functions of the probing gas in the coated and uncoated samples can be observed. The gas propagator shows a transition from a Gaussian to a non-Gaussian displacement function as a result of the increased reflections of the gas on the pore surface. As expected, a lower SNR was obtained for longer diffusion time due to  $T_1$  relaxation losses and shortened transversal relaxation times  $T_2$  and  $T_2^*$  in the nickel oxide/alumina-coated sample (Fig. 6 b).

At extended diffusion observation times (Fig. 6 b), the reduced diffusion coefficients reflect more hindrance than at  $\Delta = 5\text{ ms}$ . For the coated structure, the baseline of the gas propagator, which shows the maximum distance that molecules can travel within the time  $\Delta$ , is reached at around  $1500\mu\text{m}$  in comparison with  $2000\mu\text{m}$  for the uncoated structure.

## 5 Conclusion

A spatially resolved PFG-STE sequence was successfully applied to monolithic catalyst supports to obtain the displacement function of thermally polarized gas. The diffusion coefficients of the gas and the apparent tortuosity of the porous sponges were investigated based on the molecular interaction of the gas molecules with the pore walls in an arbitrary volume element of the porous samples for a broad range of diffusion times. While tortuosity is typically understood as a property of pores being tortuous, the apparent tortuosity serves here as a description of the influence the wall interaction has on the diffusion of the particles for a given observation time. The method

allowed diffusion studies of methane gas by measuring propagators to characterize the porous samples. The analysis of the gas propagator revealed the effect of the structure on the mean displacement of the gas molecules and the diffusion coefficients. The comparative study of coated samples with raw catalyst supports proved the potential of the method by showing even minor changes in displacement functions after adding a thin layer of washcoat on the catalyst supports, both in regular or irregular monolithic samples.

## Acknowledgment

The project was supported by the German Research Foundation (DFG) in the frame of the Research Training Group GRK 1860 "Micro-, Meso- and Macro-Porous Nonmetallic Materi-

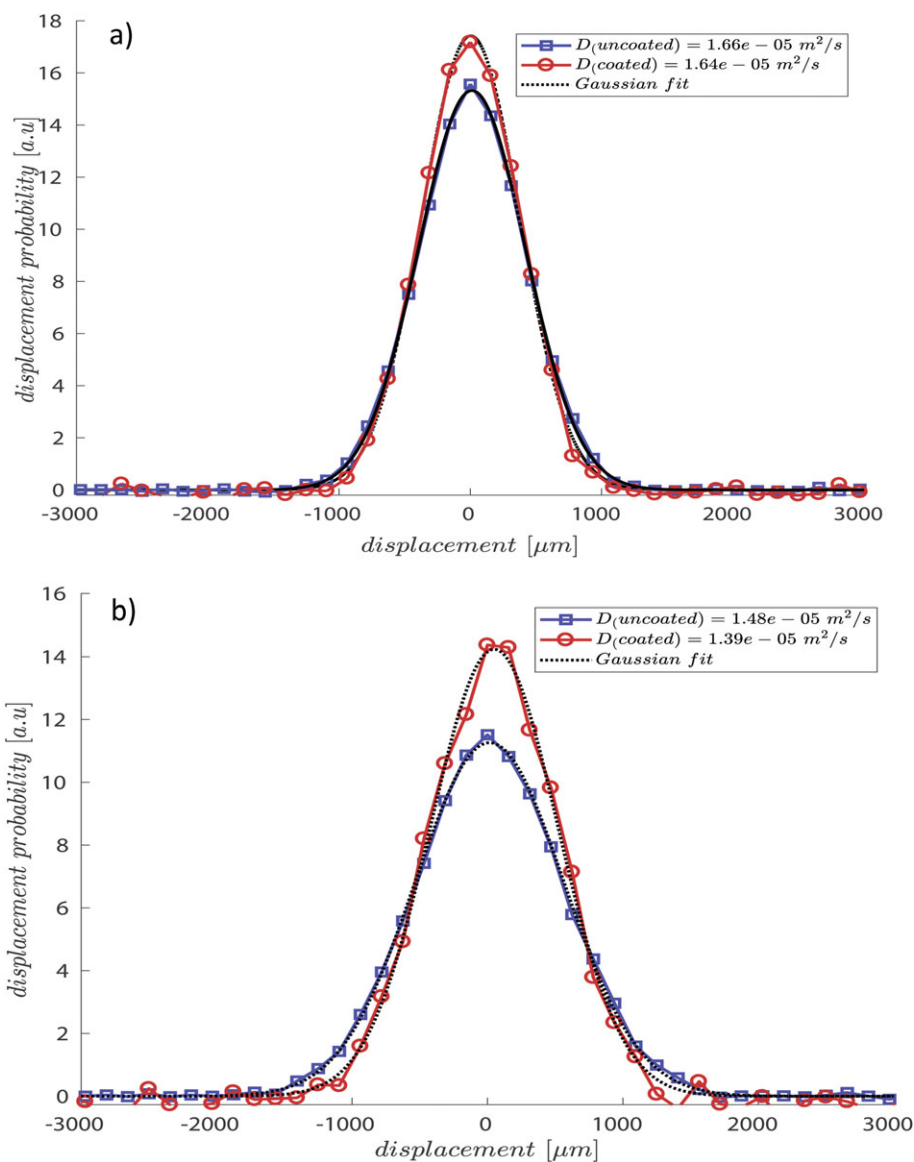


**Figure 6.** Propagators of methane in coated 20-PPI and uncoated 20-PPI sponges at (a)  $\Delta = 5\text{ ms}$  and (b)  $\Delta = 10\text{ ms}$ .

als: Fundamentals and Applications” (MIMENIMA). We are grateful to Dr. Lars Kiewidt for the characterization of the sponges and to Dr. Peter Erhard for helpful comments on the manuscript.

*The authors have declared no conflict of interest.*

## Symbols used

|                      |                                   |   |
|----------------------|-----------------------------------|---|
| $b$                  | [s mm <sup>-2</sup> ]             | $b$ -value  |
| $B_0$                | [T]                               | static magnetic field   |
| $B_1$                | [T]                               | radio frequency magnetic field  |
| $D$                  | [m <sup>2</sup> s <sup>-1</sup> ] | diffusion coefficient   |
| $G_{x,y,z}$          | [T]                               | amplitude of diffusion sensitized gradient                                |
| $P(r_0   r, \Delta)$ | [-]                               | probability density for displacement by $r$ in the time interval $\Delta$ |
| $r$                  | [m]                               | displacement  |
| $T_1$                | [s]                               | longitudinal spin relaxation time   |
| $T_2$                | [s]                               | transversal spin relaxation time  |
| $T_m$                | [s]                               | mixing time   |
| $TE$                 | [s]                               | echo time   |
| $TR$                 | [s]                               | repetition time   |

## Greek letters

|          |  |  |
|----------|--|--|
| $\delta$ | [s]                                    | duration of diffusion-sensitizing gradient |
| $\Delta$ | [s]                                    | diffusion time                             |
| $\gamma$ | [rad s <sup>-1</sup> T <sup>-1</sup> ] | gyromagnetic ratio                         |
| $\tau$   | [-]                                    | tortuosity                                 |

## Abbreviations

|      |                            |
|------|----------------------------|
| cpsi | cells per square inch      |
| FWHM | full-width half maximum    |
| MRI  | magnetic resonance imaging |
| NMR  | nuclear magnetic resonance |
| PFG  | pulsed-field gradient      |
| PPI  | pores per inch             |
| RF   | radio frequency            |
| SE   | spin echo                  |
| SNR  | signal-to-noise ratio      |
| STE  | stimulated echo            |
| TE   | echo time                  |
| TR   | repetition time            |

## References

- [1] S. L. Codd, S. A. Altobelli, *J. Magn. Reson.* **2003**, *163* (1), 16–22. DOI: [https://doi.org/10.1016/S1090-7807\(03\)00111-3](https://doi.org/10.1016/S1090-7807(03)00111-3)
- [2] W. S. Price, *NMR Studies of Translational Motion: Principles and Applications*, Cambridge University Press, Cambridge **2009**.
- [3] J. Wood, L. F. Gladden, *Appl. Catal., A* **2003**, *249* (2), 241–253. DOI: [https://doi.org/10.1016/S0926-860X\(03\)00200-X](https://doi.org/10.1016/S0926-860X(03)00200-X)
- [4] E. O. Stejskal, J. E. Tanner, *J. Chem. Phys.* **1965**, *42* (1), 288–292. DOI: <https://doi.org/10.1063/1.1695690>
- [5] R. Dawson, F. Khoury, R. Kobayashi, *AIChE J.* **1970**, *16* (5), 725–729. DOI: <https://doi.org/10.1002/aic.690160507>
- [6] L. F. Gladden, J. Mitchell, *New J. Phys.* **2011**, *13* (3), 035001. DOI: <https://doi.org/10.1088/1367-2630/13/3/035001>
- [7] M. V. Twigg, J. T. Richardson, *Ind. Eng. Chem. Res.* **2007**, *46* (12), 4166–4177. DOI: <https://doi.org/10.1021/ie061122o>
- [8] G. Groppi, E. Tronconi, *Catal. Today* **2005**, *105* (4), 297–304. DOI: <https://doi.org/10.1016/j.cattod.2005.06.041>
- [9] J. Große, B. Dietrich, H. Martin, M. Kind, J. Vicente, E. H. Hardy, *Chem. Eng. Technol.* **2008**, *31* (2), 307–314. DOI: <https://doi.org/10.1002/ceat.200700403>
- [10] C. van Gulijk, M. J. G. Linders, T. Valdés-Solís, F. Kapteijn, *Chem. Eng. J.* **2005**, *109* (1), 89–96. DOI: <https://doi.org/10.1016/j.cej.2005.03.013>
- [11] I. V. Koptuyug, L. Y. Khitrina, V. N. Parmon, R. Z. Sagdeev, *Magn. Reson. Imaging* **2001**, *19* (3–4), 531–534. DOI: [https://doi.org/10.1016/S0730-725X\(01\)00286-7](https://doi.org/10.1016/S0730-725X(01)00286-7)
- [12] J. Grosse, B. Dietrich, G. Garrido, P. Habisreuther, K. Bettina, *Ind. Eng. Chem. Res.* **2009**, *48* (23), 10395–10401. DOI: <https://doi.org/10.1021/ie900651c>
- [13] A. A. Lysova, J. A. Bergwerff, L. Espinosa-Alonso, B. M. Weckhuysen, I. V. Koptuyug, *Appl. Catal., A* **2010**, *374* (1–2), 126–136. DOI: <https://doi.org/10.1016/j.apcata.2009.11.038>
- [14] I. V. Koptuyug, L. Y. Ilyina, A. V. Matveev, R. Z. Sagdeev, V. N. Parmon, S. A. Altobelli, *Catal. Today* **2001**, *69* (1–4), 385–392. DOI: [https://doi.org/10.1016/S0920-5861\(01\)00396-0](https://doi.org/10.1016/S0920-5861(01)00396-0)
- [15] X. H. Ren, M. Bertmer, S. Stapf, *Appl. Catal., A* **2002**, *228* (1–2), 39–52. DOI: [https://doi.org/10.1016/S0926-860X\(01\)00958-9](https://doi.org/10.1016/S0926-860X(01)00958-9)
- [16] T. G. A. Youngs, D. Weber, L. F. Gladden, C. Hardacre, *J. Phys. Chem.* **2009**, *113* (51), 21342–21352. DOI: <https://doi.org/10.1021/jp906677c>
- [17] M. H. Haider, C. D’Agostino, N. F. Dummer, et al., *Chemistry* **2014**, *20*, 1743–1752. DOI: <https://doi.org/10.1002/chem.201302348>
- [18] C. D’Agostino, Y. Ryabenkova, P. J. Miedziak, et al., *Catal. Sci. Technol.* **2014**, *4*, 1313–1322. DOI: <https://doi.org/10.1039/C4CY00027G>
- [19] Y. Zhang, L. Xiao, G. Liao, Y. Q. Song, *J. Magn. Reson.* **2016**, *269*, 196–202. DOI: <https://doi.org/10.1016/j.jmr.2016.06.013>
- [20] M. Terekhov, D. Höpfel, *Chem. Eng. Technol.* **2006**, *29* (7), 807–815. DOI: <https://doi.org/10.1002/ceat.200600053>
- [21] E. H. Hardy, *Chem. Eng. Technol.* **2006**, *29* (7), 785–795. DOI: <https://doi.org/10.1002/ceat.200600046>
- [22] A. Caprihan, C. F. M. Clewett, D. O. Kuethe, E. Fukushima, S. J. Glass, *Magn. Reson. Imaging* **2001**, *19* (3–4), 311–317. DOI: [https://doi.org/10.1016/S0730-725X\(01\)00242-9](https://doi.org/10.1016/S0730-725X(01)00242-9)
- [23] S. D. Beyea, S. L. Codd, D. O. Kuethe, E. Fukushima, *Magn. Reson. Imaging* **2003**, *21* (3–4), 201–205. DOI: [https://doi.org/10.1016/S0730-725X\(03\)00125-5](https://doi.org/10.1016/S0730-725X(03)00125-5)
- [24] I. V. Koptuyug, S. A. Altobelli, E. Fukushima, A. V. Matveev, R. Z. Sagdeev, *J. Magn. Reson.* **2000**, *147* (1), 36–42. DOI: <https://doi.org/10.1006/jmre.2000.2186>
- [25] J. E. Tanner, *J. Chem. Phys.* **1970**, *52* (5), 2523–2526. DOI: <https://doi.org/10.1063/1.1673336>
- [26] M. Valentini, *Organometallics* **2000**, *19* (13), 2551–2555. DOI: <https://doi.org/10.1021/om000104i>
- [27] F. Stallmach, J. Kärger, *Adsorption* **1999**, *133* (2), 117–133. DOI: <https://doi.org/10.1023/A:1008949607093>

- [28] N. Hedin, G. J. DeMartin, K. G. Strohmaier, S. C. Reyes, *Microporous Mesoporous Mater.* **2007**, *98* (1–3), 182–188. DOI: <https://doi.org/10.1016/j.micromeso.2006.08.017>
- [29] A. Haase, J. Frahm, D. Matthaei, W. Hänicke, K. D. Merboldt, *J. Magn. Reson.* **1986**, *67* (2), 258–266. DOI: [https://doi.org/10.1016/0022-2364\(86\)90433-6](https://doi.org/10.1016/0022-2364(86)90433-6)
- [30] R. Kimmich, F. Winter, W. Nusser, K. H. Spohn, *J. Magn. Reson.* **1986**, *68* (2), 263–282. DOI: [https://doi.org/10.1016/0022-2364\(86\)90243-X](https://doi.org/10.1016/0022-2364(86)90243-X)
- [31] I. Tkáč, Z. Starčuk, I. Y. Choi, R. Gruetter, *Magn. Reson. Med.* **1999**, *41* (4), 649–656. DOI: [https://doi.org/10.1002/\(SICI\)1522-2594\(199904\)41:4<649::AID-MRM2>3.0.CO;2-G](https://doi.org/10.1002/(SICI)1522-2594(199904)41:4<649::AID-MRM2>3.0.CO;2-G)
- [32] D. G. Cory, A. N. Garroway, *Magn. Reson. Med.* **1990**, *14* (3), 435–444. DOI: <https://doi.org/10.1002/mrm.1910140303>
- [33] P. T. Callaghan, D. MacGowan, K. J. Packer, F. O. Zelaya, *J. Magn. Reson.* **1990**, *90* (1), 177–182. DOI: [https://doi.org/10.1016/0022-2364\(90\)90376-K](https://doi.org/10.1016/0022-2364(90)90376-K)
- [34] B. Soher, D. Semanchuk, D. Todd, J. Steinberg, K. Young, *19th Annual Meeting ISMRM*, Montréal, QC, May **2011**.
- [35] J. Winkelmann, *Gases in Gases, Liquids and Their Mixtures* (Ed: M. D. Lechner), Springer, Basel **2007**. DOI: <https://doi.org/10.1007/978-3-540-49718-9>
- [36] A. H. Kristensen, A. Thorbjørn, M. P. Jensen, M. Pedersen, P. Moldrup, *J. Contam. Hydrol.* **2010**, *115* (1–4), 26–33. DOI: <https://doi.org/10.1016/j.jconhyd.2010.03.003>
- [37] P. Habisreuther, N. Djordjevic, N. Zarzalis, *Chem. Eng. Sci.* **2009**, *64* (23), 4943–4954. DOI: <https://doi.org/10.1016/j.ces.2009.07.033>
- [38] J. Vicente, F. Topin, J.-V. Daurelle, *Mater. Trans.* **2006**, *47* (9), 2195–2202. DOI: <https://doi.org/10.2320/matertrans.47.2195>
- [39] L. Kiewidt, *Solid Sponges as Support for Heterogeneous Catalysts in Gas-Phase Reactions*, Ph.D. Thesis, University of Bremen **2018**.